Cosmological implications of the full shape of anisotropic clustering measurements in BOSS and eBOSS

Agne Semenaite [ORCID],[1]★ Ariel G. Sánchez [ORCID],[1,2] Andrea Pezzotta,[1] Jiamin Hou,[1,3] Roman Scoccimarro,[4] Alexander Eggemeier,[5] Martin Crocce [ORCID],[6,7] Chia-Hsun Chuang [ORCID],[8] Alexander Smith,[9] Cheng Zhao,[10] Joel R. Brownstein [ORCID],[11] Graziano Rossi[12] and Donald P. Schneider[13,14]

[1]*Max-Planck-Institut für extraterrestrische Physik, Postfach 1312, Giessenbachstr, D-85748 Garching, Germany*
[2]*Fakultät für Physik, Ludwig-Maximilians Universität, Universitäs-Sternwarte Müchen, Scheinerstrasse 1, D-81679 Müchen, Germany*
[3]*Department of Astronomy, University of Florida, 211 Bryant Space Science Center, Gainesville, FL 32611, USA*
[4]*Center for Cosmology and Particle Physics, Department of Physics, New York University, NY 10003, New York, USA*
[5]*Institute for Computational Cosmology, Department of Physics, Durham University, South Road, Durham DH1 3LE, UK*
[6]*Institute of Space Sciences (ICE, CSIC), Campus UAB, Carrer de Can Magrans, s/n, E-08193 Barcelona, Spain*
[7]*Institut d'Estudis Espacials de Catalunya (IEEC), E-08034 Barcelona, Spain*
[8]*Kavli Institute for Particle Astrophysics and Cosmology, Stanford University, 452 Lomita Mall, Stanford, CA 94305, USA*
[9]*IRFU, CEA, Université Paris-Saclay, F-91191 Gif-sur-Yvette, France*
[10]*Institute of Physics, Laboratory of Astrophysics, École Polytechnique Fédérale de Lausanne (EPFL), Observatoire de Sauverny, CH-1290 Versoix, Switzerland*
[11]*Department of Physics and Astronomy, University of Utah, 115 S. 1400 E., Salt Lake City, UT 84112, USA*
[12]*Department of Physics and Astronomy, Sejong University, Seoul 143-747, Republic of Korea*
[13]*Department of Astronomy and Astrophysics, The Pennsylvania State University, University Park, PA 16802, USA*
[14]*Institute for Gravitation and the Cosmos, The Pennsylvania State University, University Park, PA 16802, USA*

ABSTRACT

We present the analysis of the full shape of anisotropic clustering measurement from the extended Baryon Oscillation Spectroscopic Survey (eBOSS) quasar sample together with the combined galaxy sample from the Baryon Oscillation Spectroscopic Survey (BOSS), re-analysed using an updated recipe for the non-linear matter power spectrum and the non-local bias parameters. We obtain constraints for flat Lambda cold dark matter cosmologies, focusing on the cosmological parameters that are independent of the Hubble parameter h. Our recovered value for the Root Mean Square (RMS) linear perturbation theory variance as measured on the scale of 12 Mpc is $\sigma_{12} = 0.805 \pm 0.049$, while using the traditional reference scale of $8\,h^{-1}$ Mpc gives $\sigma_8 = 0.815 \pm 0.044$. We quantify the agreement between our measurements and the latest cosmic microwave background data from *Planck* using the suspiciousness metric, and find them to be consistent within $0.64 \pm 0.03\sigma$. Combining our clustering constraints with the 3×2pt data sample from the Dark Energy Survey Year 1 release slightly degrades this agreement to the level of $1.54 \pm 0.08\sigma$, while still showing an overall consistency with *Planck*. We furthermore study the effect of imposing a *Planck* – like prior on the parameters that define the shape of the linear matter power spectrum, and find significantly tighter constraints on the parameters that control the evolution of density fluctuations. In particular, the combination of low-redshift data sets prefers a value of the physical dark energy density $\omega_{DE} = 0.335 \pm 0.011$, which is 1.7σ higher than the one preferred by *Planck*.

Key words: cosmological parameters – large-scale structure of Universe.

1 INTRODUCTION

The rapid progress of observational cosmology in recent years has been fuelled by an abundance of accurate observations (Riess et al. 1998; Perlmutter et al. 1999; Cole et al. 2005; Eisenstein et al. 2005; Anderson et al. 2012; Hinshaw et al. 2013; Alam et al. 2017, 2021; Planck Collaboration VI 2020). The Lambda cold dark matter (ΛCDM) model has emerged as the new cosmological

paradigm, being able to simultaneously describe all state-of-the-art observations. However, the two components making up the majority of the total energy budget of the Universe today in this model, dark energy and dark matter, remain poorly understood.

As it provides the most precise parameter constraints to date, the best-fitting ΛCDM model to the cosmic microwave background (CMB) observations by the *Planck* satellite (Planck Collaboration VI 2020) has become the synonym to 'standard cosmological model'. The comparison of predictions for the expansion history of the Universe $H(z)$, and the rate at which cosmic structures form at later times $f(z)$ with observations at lower redshifts serves as

★ E-mail: agne@mpe.mpg.de

a powerful test of the ΛCDM paradigm. While a broad range of observations are in agreement with the CMB predictions, the increasingly precise measurements from the cosmic distance ladder (Riess et al. 2018, 2019), as well as the ever-increasing weak gravitational lensing data sets (Hildebrandt et al. 2016; Abbott et al. 2018; Hikage et al. 2019), display hints of tension with *Planck* ΛCDM. In particular, local direct probes seem to prefer an up to 5σ (Riess et al. 2021) greater expansion rate of the Universe (the 'H_0 tension') while, less significantly (up to 3σ; Heymans et al. 2021), weak gravitational lensing measurements exhibit a lower amplitude (the 'σ_8 tension') than predicted by *Planck*. There is still no conclusive evidence on what drives these differences in the recovered values, and it is not uncommon for proposed solutions to the H_0 tension to make the σ_8 tension worse (see e.g. Hill et al. 2020).

With the lack of consensus on where (and whether) the inconsistencies with *Planck* ΛCDM arise, the cosmological community has put in an increased effort in assessing the internal consistency between different data sets within the ΛCDM scenario. Galaxy clustering allows to probe and distinguish how the underlying cosmology affects the background expansion of the Universe and its effects on the structure growth through baryon acoustic oscillations (BAO) and redshift-space distortions (RSD). Both of these effects set important features of the two-point correlation function, which can be fit to obtain summary statistics that carry compressed cosmological information. BAO set the angular scale of the acoustic peak, allowing to probe the distance – redshift relation. On the other hand, RSD provide information about structure growth through galaxy peculiar velocities, whose effect on the amplitude of the power spectrum is commonly characterized by the product of the logarithmic growth rate f and the RMS linear perturbation theory variance σ_8 (although see Sánchez 2020, for the problems caused by this approach). While analyses based solely on RSD and BAO summary statistics allow excellent internal consistency tests and may help constrain beyond – ΛCDM scenarios, it has been shown that they do not preserve all the information of the full measurement, in particular, losing the additional constraining power available from its shape (Brieden, Gil-Marín & Verde 2021).

Other analyses therefore make use of the information recovered from fitting the full shape of two-point clustering measurements, either in Fourier or configuration space, directly comparing models against data (d'Amico et al. 2020; Ivanov, Simonović & Zaldarriaga 2020; Tröster et al. 2020; Chen, Vlah & White 2022). These analyses tend to lose some of the immediate interpretability of the summary statistics but instead allow to directly obtain constraints of cosmological parameters independently of external data sets. This type of analyses have therefore recently received attention as a way to test the consistency between large-scale structure (LSS) and CMB measurements.

Tröster et al. (2020) showed that the full shape analysis of galaxy clustering produces cosmological constraints that are comparable to those of other low-redshift probes. This work followed the analysis of correlation function wedges of Baryon Oscillation Spectroscopic Survey (BOSS) galaxies by Sánchez et al. (2017) in order to derive constraints on flat ΛCDM cosmologies from galaxy clustering alone (i.e. without combining it with CMB measurements, as was done in the BOSS Data Release 12 consensus analysis; Alam et al. 2017). Furthermore, the work also presented joint low-redshift constraints by combining galaxy clustering with weak lensing measurements from the Kilo-Degree Survey (KV450).

The σ_8 value recovered from the full shape analysis of the correlation function wedges by Tröster et al. (2020) is 2.1σ low compared to *Planck*'s prediction, with the difference increasing to 3.4σ when weak lensing measurements from KV450, are added, indicating that there may be some consistent discrepancy between CMB predictions and low-redshift observations. This is also consistent with the more recent analysis by Heymans et al. (2021) where BOSS galaxies are used as lenses in the so-called '3 × 2pt' analysis (a set of three correlation functions consisting of autocorrelation of the lens galaxy positions, source galaxy shapes, and the cross-correlation of the two), which finds a $\sim 3\sigma$ discrepancy with *Planck*'s value of $S_8 = \sigma_8\sqrt{\Omega_m/0.3}$, that combines σ_8 with the matter density Ω_m in a way that minimizes correlation between the two parameters. This result is consistent with the findings from other major weak lensing surveys [Dark Energy Survey (DES Collaboration 2021) and Hyper Suprime-Cam (Hikage et al. 2019)], even though, most recently, DES reported consistency between their 3 × 2pt ΛCDM constraints and those of *Planck* when the full parameter space is considered. Furthermore, σ_8 may not be an entirely appropriate parameter for assessing consistency among the different surveys, as Sánchez (2020) has shown that it is affected by the different posterior distributions of Hubble parameter h recovered by different analyses. Alternatively, one may define σ_{12} – the variance as measured on a fixed scale of 12 Mpc. In this work, we adopt this notation and use σ_{12} to both accurately characterize the amplitude of the power spectrum today as well as assess the consistency among the probes considered.

In this work, we are therefore interested in building upon Tröster et al. (2020) and exploring, whether the discrepancy between the low-redshift probes and *Planck* within the ΛCDM model holds when extending the redshift range probed by the clustering measurements with the addition of extended Baryon Oscillation Spectroscopic Survey (eBOSS) quasar clustering. We provide the joint constraints from the full shape analysis of BOSS galaxy and eBOSS quasar clustering on their own, as well as in combination with weak lensing information. For our weak lensing data set, we use the 3 × 2pt measurements from the Dark Energy Survey Year 1 (DES Y1; Abbott et al. 2018) release, which both cover a larger area than KV450 and include galaxy clustering and galaxy–galaxy lensing as well as the shear-only measurements. If the tension seen between the low-redshift probes and *Planck* is purely statistical, adding more data should not only tighten the posterior contours but be able to bring the constraints to a better agreement. The results from an equivalent analysis with KiDS-450 shear measurements are available in Appendix A.

In addition to expanding our data sets, we also aim to re-define the parameter space following Sanchez et al. (2021), who distinguish 'shape' and 'evolution' cosmological parameters. This classification is introduced to describe the degenerate way in which evolution parameters affect the linear matter power spectrum when expressed in Mpc units. In such parameter space, σ_8 is replaced by σ_{12}, as discussed above, and the relative matter and dark energy densities (Ω_m, Ω_{DE}) are replaced by their physical counterparts (ω_m, ω_{DE}). While in Sanchez et al. (2021), the h-independent parameter space is presented to create a framework that allows them to reduce the number of parameters required to model the cosmology dependence of the matter power spectrum, the advantage of such parameter choice for this work is two-fold. First, the derived constraints do not depend on the posterior of h of the particular analysis and can therefore be directly compared with constraints from other data sets and, second, the effect that each of the parameters has on the power spectrum is clear, with evolution parameters affecting its amplitude and shape parameters determining the shape.

We provide a more detailed description of the parameter space we use (including the prior choices) in Section 2, together with a summary of our data and models, and illustrate how it compares with its h-dependent equivalent in Section 3.1, where we also present our cosmological constraints from BOSS and eBOSS. The results obtained when adding DES are further presented in Section 3.3 We finish with a discussion of our results in Section 4 and present our conclusions in Section 5.

2 METHODOLOGY

This work is an extension of Tröster et al. (2020) and largely follows the same structure and methods – we assume flat ΛCDM cosmology and obtain the joint low-redshift parameter constraints by combining the likelihoods for each data set considered independently. Our model for anisotropic galaxy and quasar clustering measurements follows that described in Sánchez et al. (2017) for the so-called full shape analysis (with the exception of the matter power spectrum model) whereas for the '3 × 2pt' analysis (galaxy shear, galaxy–galaxy lensing, and galaxy clustering) we use the model described in Abbott et al. (2018). In this section, we summarize the data and models used with a more detailed description available in the references above. The measurements here are as used in the respective original analyses and therefore had been tested against various systematics and include the appropriate corrections.

2.1 Galaxy and QSO clustering measurements

The Sloan Digital Sky Survey (SDSS) has mapped the LSS of the Universe thanks to the accurate measurements by the double-armed spectrographs (Smee et al. 2013) at the Sloan Foundation Telescope at Apache Point Observatory (Gunn et al. 2006). Throughout its different stages (York et al. 2000; Eisenstein et al. 2011; Blanton et al. 2017), the SDSS has provided redshift information on millions of galaxies and quasars.

We consider clustering measurements in configuration space from two data sets: the galaxy samples of BOSS (Dawson et al. 2013), corresponding to SDSS DR12 (Alam et al. 2015; Reid et al. 2016), and the QSO catalogue (Lyke et al. 2020) from eBOSS (Dawson et al. 2016), contained in SDSS DR16 (Ahumada et al. 2020; Ross et al. 2020). In each case, the information from the full anisotropic correlation function $\xi(s, \mu)$, where s denotes the comoving pair separation and μ represents the cosine of the angle between the separation vector and the line of sight, was compressed into different but closely related statistics.

We analyse the clustering properties of the combined BOSS galaxy sample using the measurements of Sánchez et al. (2017), who employ the clustering wedges statistic (Kazin, Sánchez & Blanton 2012), $\xi_{\Delta\mu}(s)$, which corresponds to the average of $\xi(s, \mu)$, over the interval $\Delta\mu = \mu_2 - \mu_1$, that is

$$\xi_{\Delta\mu}(s) = \frac{1}{\Delta\mu} \int_{\mu_1}^{\mu_2} \xi(\mu, s) \, d\mu. \tag{1}$$

Sánchez et al. (2017) measured three wedges by splitting the μ range from 0 to 1 into three equal-width intervals. We consider their measurements in two redshift bins, with $0.2 < z < 0.5$ (the LOWZ sample) and $0.5 < z < 0.75$ (CMASS), corresponding to the effective redshifts $z_{\rm eff} = 0.38$ and 0.61, respectively. The covariance matrices, **C**, of these data were estimated using the set of 2045 MD-PATCHY mock catalogues described in Kitaura et al. (2016). These measurements were also used in the analysis of Tröster et al. (2020)

and the recent studies of the cosmological implications of the KiDS 1000 data set (Heymans et al. 2021; Tröster et al. 2021).

For the eBOSS QSO catalogue, we use the measurements of Hou et al. (2021), who considered the Legendre multipoles given by

$$\xi_\ell(s) = \frac{2\ell + 1}{2} \int_{-1}^{1} \xi(\mu, s) \mathcal{L}_\ell(\mu) \, d\mu, \tag{2}$$

where $\mathcal{L}_\ell(\mu)$ denotes the ℓ-th order Legendre polynomial. We consider the multipoles $\ell = 0, 2, 4$ obtained using the redshift range $0.8 < z < 2.2$, with an effective redshift $z_{\rm eff} = 1.48$. The covariance matrix of these measurements were obtained using the set of 1000 mock catalogues described in Zhao et al. (2021). Besides the QSO sample used here, the full eBOSS data set contains two additional tracers, the luminous red galaxy and emission line galaxy samples (for the corresponding BAO and RSD analyses, see Gil-Marín et al. 2020; Tamone et al. 2020; Bautista et al. 2021; de Mattia et al. 2021). These samples overlap in redshift among them and with the galaxies from BOSS. We therefore restrict our analysis of eBOSS data to the QSO sample to, in combination with BOSS, cover the maximum possible redshift range while ensuring that the clustering measurements can be treated as independent in our likelihood analysis.

We treat the measurements from BOSS and eBOSS as in the original analyses of Sánchez et al. (2017) and Hou et al. (2021). We restrict our analysis to pair separations within the range $20 \, h^{-1}$ Mpc $< s <$ $160 \, h^{-1}$ Mpc. We assume a Gaussian likelihood for each set of measurements, in which the covariance matrices are kept fixed. We account for the impact of the finite number of mock catalogues used to derive **C** (Kaufman 1967; Hartlap, Simon & Schneider 2007; Percival et al. 2014). The large number of mock catalogues used ensures that the effect of the noise in **C** on the obtained cosmological constraints corresponds to a modest correction factor of less than 2 per cent.

2.2 Modelling anisotropic clustering measurements

Our modelling of the full shape of the Legendre multipoles and clustering wedges of the anisotropic two-point correlation function largely follows the treatment of Sánchez et al. (2017), with some important differences.

We compute model predictions of the non-linear matter power spectrum, $P_{\rm mm}(k)$, using the Rapid and Efficient SPectrum calculation based on RESponSe functiOn approach (RESPRESSO; Nishimichi, Bernardeau & Taruya 2017). The key ingredient of RESPRESSO is the response function, $K(k, q)$, which quantifies the variation of the non-linear matter power spectrum at scale k induced by a change of the linear power at scale q as

$$K(k, q) \equiv q \frac{\partial P_{\rm mm}(k)}{\partial P_{\rm L}(q)}. \tag{3}$$

Nishimichi, Bernardeau & Taruya (2016) presented a phenomenological model for $K(k, q)$ based on renormalized perturbation theory (Taruya et al. 2012), which gives a good agreement with simulation results over a wide range of scales for k and q. The response function allows to obtain $P_{\rm mm}(k)$ for arbitrary cosmological parameters $\boldsymbol{\theta}$ based on a measurement from N-body simulations of a fiducial cosmology $\boldsymbol{\theta}_{\rm fid}$ as

$$P_{\rm mm}(k|\boldsymbol{\theta}) = P_{\rm mm}(k|\boldsymbol{\theta}_{\rm fid}) \int d \ln q \, K(k, q)$$
$$\times [P_{\rm L}(q|\boldsymbol{\theta}) - P_{\rm L}(q|\boldsymbol{\theta}_{\rm fid})]. \tag{4}$$

The choice of $\boldsymbol{\theta}_{\mathrm{fid}}$ in RESPRESSO corresponds to the best-fitting ΛCDM model to the *Planck* 2015 data (Planck Collaboration XIII 2016). Equation (4) is most accurate for cosmologies that are close to $\boldsymbol{\theta}_{\mathrm{fid}}$. For cosmologies further away from the fiducial, its accuracy can be improved by performing a multistep reconstruction. Eggemeier et al. (2020) showed that RESPRESSO outperforms other perturbation theory based models in terms of the range of validity and accurate recovery of mean posterior values.

Following the notation of Eggemeier, Scoccimarro & Smith (2019), we describe the relation between the galaxy density fluctuations, δ, and the matter density fluctuations, δ_{m}, at one loop in terms of the four-parameter model

$$\delta = b_1 \delta_m + \frac{b_2}{2} \delta_m^2 + \gamma_2 \mathcal{G}_2(\Phi_v) + \gamma_{21} \mathcal{G}_2(\varphi_1, \varphi_2) + ..., \quad (5)$$

where the first two terms represent contributions from linear and quadratic local bias, while the remaining ones correspond to non-local terms. Here, $\mathcal{G}_2$ is the Galileon operator of the normalized velocity potential Φ_v, and φ_1 is the linear Lagrangian perturbation potential with φ_2 as a second-order potential that accounts for the non-locality of the gravitational evolution,

$$\mathcal{G}_2(\Phi_v) = (\nabla_{ij}\Phi_v)^2 - (\nabla^2\Phi_v)^2, \quad (6)$$

$$\mathcal{G}_2(\varphi_1, \varphi_2) = \nabla_{ij}\varphi_2 \nabla_{ij}\varphi_1 - \nabla^2\varphi_2 \nabla^2\varphi_1. \quad (7)$$

Two-point statistics alone do not constrain γ_2 well, because γ_2 enters at higher order and is degenerate with γ_{21}. Therefore, we set the value of this parameter in terms of the linear bias b_1 using the quadratic relation

$$\gamma_2(b_1) = 0.524 - 0.547b_1 + 0.046b_1^2, \quad (8)$$

which describes the results of Sheth, Chan & Scoccimarro (2013) using excursion set theory. Eggemeier et al. (2020) showed that this relation is more accurate for tracers with $b_1 \gtrsim 1.3$ than the one obtained under the assumption of local bias in Lagrangian space used in Sánchez et al. (2017).

The value of γ_{21} can also be derived in terms of b_1 under the assumption of the conserved evolution of galaxies (hereafter co-evolution) after their formation as (Fry 1996; Catelan et al. 1998; Catelan, Porciani & Kamionkowski 2000; Chan, Scoccimarro & Sheth 2012)

$$\gamma_{21} = -\frac{2}{21}(b_1 - 1) + \frac{6}{7}\gamma_2. \quad (9)$$

This relation was thoroughly tested against constraints derived from a combination of power spectrum and bispectrum data in Eggemeier et al. (2021), and found to be in excellent agreement for BOSS galaxies. In addition to this, in Section 2.5, we confirm that the use of this relation gives an accurate description of the results of N-body simulations and we therefore implement it in our analysis of the BOSS and eBOSS data. In this way, the only required free bias parameters in our recipe are b_1 and b_2, while the non-local bias terms can be fully expressed in terms of the linear bias through equations (8) and (9).

Our description of the effects of RSD matches that of Sánchez et al. (2017). Following Scoccimarro (2004) and Taruya, Nishimichi & Saito (2010), we write the 2D redshift-space power spectrum as

$$P(k, \mu) = W_\infty(ifk\mu) P_{\mathrm{novir}}(k, \mu), \quad (10)$$

where the 'no-virial' power spectrum, $P_{\mathrm{novir}}(k, \mu)$, is computed using the one-loop approximation and includes three terms, one representing a non-linear version of the Kaiser formula (Kaiser 1987)

and two higher-order terms that include the contributions of the cross-spectrum and bispectrum between densities and velocities. Besides the non-linear matter power spectrum, $P_{\mathrm{novir}}(k, \mu)$ requires also the velocity–velocity and matter–velocity power spectra, which we compute using the empirical relations measured from N-body simulations of Bel et al. (2019). The function $W_\infty(\lambda = ifk\mu)$ represents the large-scale limit of the generating function of the pairwise velocity distribution, which accounts for non-linear corrections due to fingers of God or virial motions and can be parametrized as (Sánchez et al. 2017)

$$W_\infty(\lambda) = \frac{1}{\sqrt{1 - \lambda^2 a_{\mathrm{vir}}^2}} \exp\left(\frac{\lambda^2 \sigma_v^2}{1 - \lambda^2 a_{\mathrm{vir}}^2}\right), \quad (11)$$

where a_{vir} is a free parameter characterizing the kurtosis of the small-scale velocity distribution, and σ_v is the 1D linear velocity dispersion defined in terms of the linear matter power spectrum as

$$\sigma_v^2 \equiv \frac{1}{6\pi^2} \int \mathrm{d}k\, P_{\mathrm{L}}(k). \quad (12)$$

The QSO sample is known to be affected by non-negligible redshift errors that also affect the clustering measurements (Zarrouk et al. 2018). We account for this following Hou et al. (2018), who showed that this effect can be correctly described by including an additional damping factor to the power spectrum of equation (10) of the form $\exp(-k\mu\sigma_{\mathrm{err}})$, where σ_{err} is treated as an additional free parameter.

Finally, the Alcock–Paczynski distortions (Alcock & Paczyński 1979) due to the difference between the true and fiducial cosmologies are accounted for by introducing the geometric distortion factors

$$q_\perp = D_{\mathrm{M}}(z_{\mathrm{eff}})/D_{\mathrm{M}}'(z_{\mathrm{eff}}), \quad (13)$$

$$q_\parallel = H'(z_{\mathrm{eff}})/H(z_{\mathrm{eff}}). \quad (14)$$

Here, $D_{\mathrm{M}}(z)$ is the comoving angular diameter distance and $H(z)$ is the Hubble parameter, with primed quantities corresponding to the fiducial cosmology used to convert redshifts to distances. The distortion factors are then applied to rescale the separations s of galaxy pairs and the angles between the separation vector and the line-of-sight μ such that

$$s = s'\left(q_\parallel^2 \mu'^2 + q_\perp^2\left(1 - \mu'^2\right)\right), \quad (15)$$

$$\mu = \mu' \frac{q_\parallel}{\sqrt{q_\parallel^2 \mu'^2 + q_\perp^2(1 - \mu'^2)}}. \quad (16)$$

In summary, our model of the clustering wedges from BOSS requires three free parameters, b_1, b_2, and a_{vir}, with the values of γ_2 and γ_{21} given in terms of b_1 using equations (8) and (9). This is one less free parameter than in the original analysis of Sánchez et al. (2017). The Legendre multipoles of the eBOSS QSO require the addition of σ_{err}, leading to a total of four free parameters.

2.3 Additional data sets

We complement the information from our clustering measurements with the $3 \times 2pt$ measurements from DES Y1 (Abbott et al. 2018). We also use the shear measurements from the Kilo-Degree Survey (KiDS-450; Hildebrandt et al. 2016) and present the results in Appendix A.

The source galaxy samples from DES are split into four redshift bins, spanning the redshift range of $0.2 < z \le 1.3$. In addition to shear measurements from the source galaxies, the DES Y1 data set also includes galaxy clustering and galaxy–galaxy lensing two-point correlation function measurements, as well as the lens redshift

distributions for five redshift bins in the range of $0.15 < z < 0.9$. Our scale cuts for these measurements match those of Abbott et al. (2018).

For our 3×2pt analysis, we use the DES likelihood as implemented in CosmoMC (Lewis & Bridle 2002), which corresponds to the model described in Abbott et al. (2018). The likelihood includes models for the two-point correlation functions describing galaxy–galaxy lensing, galaxy clustering, and cosmic shear. The correlation functions are modelled by making use of Limber and flat-sky approximations (Limber 1954; Kaiser 1992; LoVerde & Afshordi 2008; Kilbinger et al. 2017) with the non-linear power spectrum obtained using HMCODE (Mead et al. 2015) as implemented in CAMB (Lewis, Challinor & Lasenby 2000). The smallest angular separations considered correspond to a comoving scale of $8\,h^{-1}$ Mpc. The intrinsic alignment is modelled using a 'non-linear linear' alignment recipe (Hirata & Seljak 2004; Bridle & King 2007). The model also includes a treatment for multiplicative shear bias and photometric redshift uncertainty. The former is accounted for by introducing multiplicative bias terms of the form $(1 + m^i)$ for each bin i for shear and galaxy–galaxy lensing. The latter is modelled by the shift parameters δz^i assigned to each bin for both source and lens galaxies. Finally, baryonic effects are not included as they are expected to be below the measurement errors for the range of scales considered in the analysis. For all the weak lensing nuisance parameters, we impose the same priors as the ones listed in Abbott et al. (2018).

Additionally, we test the consistency of the low-redshift LSS measurements with the latest CMB temperature and polarization power spectra from the *Planck* satellite (Planck Collaboration VI 2020), to which we refer simply as '*Planck*'. We do not include CMB lensing information. We use the public nuisance parameter-marginalized likelihood `plik_lite_TTTEEE+lowl + lowE` for all *Planck* constraints (Planck Collaboration VI 2020).

2.4 Parameter spaces and prior ranges

Our goal is to obtain constraints on the parameters of the standard ΛCDM model, which corresponds to a flat universe, where dark energy is characterized by a constant equation of state parameter $w_{DE} = -1$. Following Sanchez et al. (2021), we focus on cosmological parameters that can be classified as either 'shape' or 'evolution'. The former are parameters that control the shape of the linear-theory power spectrum expressed in Mpc units. The latter only affect the amplitude of $P_L(k)$ at any given redshift. Assuming a fixed total neutrino mass of $\sum m_\nu = 0.06$ eV, the ΛCDM model can be described by the parameters

$$\boldsymbol{\theta} = (\omega_b, \omega_c, \omega_{DE}, A_s, n_s). \tag{17}$$

These are the present-day physical energy densities of baryons, cold dark matter, and dark energy, and the amplitude and spectral index of the primordial power spectrum of scalar perturbations at the pivot wavenumber of $k_0 = 0.05\,\text{Mpc}^{-1}$.

Additional parameters can be derived from the set of equation (17). The dimensionless Hubble parameter, h, is defined by the sum of all energy contributions. For a ΛCDM model, this is

$$h^2 = \omega_b + \omega_c + \omega_\nu + \omega_{DE}. \tag{18}$$

It is also common to express the contributions of the various energy components in terms of the density parameters

$$\Omega_i = \omega_i / h^2, \tag{19}$$
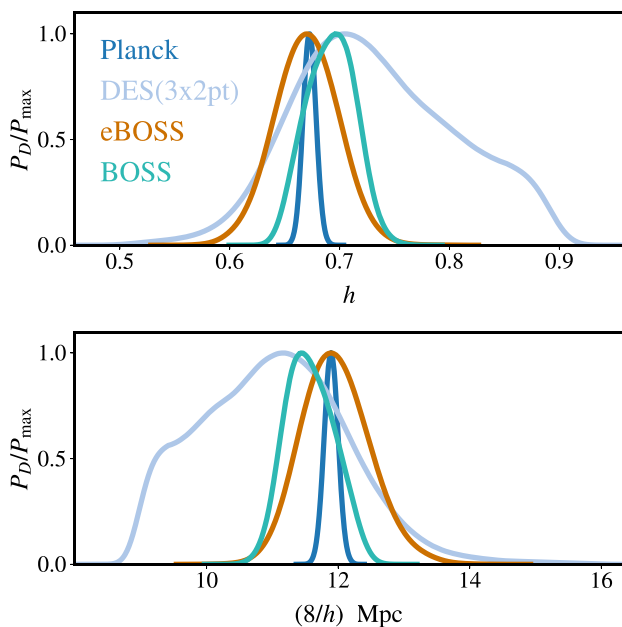
Figure 1. Upper panel 1D marginalized posteriors for h for the different data sets considered in this work (with the priors used in this analysis). Lower panel: the corresponding posteriors of the physical value of $(8/h)\,\text{Mpc}$ – the scale used to define σ_8. Any distance defined in h^{-1} Mpc units will correspond to a range of physical scales, as determined by the posterior of h. If the posterior is prior limited, as is the case with weak lensing, the choice of prior will also influence the range of physical scales that contribute to σ_8. On the other hand, the effect is much smaller for the case of narrow Gaussian h-posterior – for *Planck* σ_8 will correspond to a scale of 12 Mpc.

which represent the fraction of the total energy density of the Universe corresponding to a given component i. The overall amplitude of matter density fluctuations is often characterized in terms of σ_8, the linear-theory RMS mass fluctuations in spheres of radius $R = 8\,h^{-1}$ Mpc. A common property of these parameters is their dependence on the value of h. The issues associated with this dependence are discussed in detail by Sánchez (2020) and can be summarized as follows.

The main consequence of using quantities that depend on h in cosmological analyses is that this complicates the comparison of constraints derived from probes that lead to different posterior distributions on h. This can be illustrated most straightforwardly when considering σ_8, which is defined in terms of a scale in h^{-1} Mpc units. As done by Sánchez (2020), the 1D marginalized posterior distribution for h can be used to obtain the corresponding posterior for $(8/h)\,\text{Mpc}$ to explore what physical distances this radius corresponds to. Fig. 1 repeats this simple exercise for the data sets considered in this work – as expected, the range of scales recovered in each case heavily depends on the type of probe considered (*Planck* displaying an extremely narrow posterior at the physical scale of approximately 12 Mpc, while the remaining probes cover varying ranges), especially in the case where the posterior of h is simply limited by the prior imposed, as is the case for weak lensing data sets.

The solid line in Fig. 2 shows the density field variance σ_R as a function of the scale R in a *Planck* ΛCDM Universe. The shaded areas indicate the range of physical scales covered by the posterior distributions of $(8/h)\,\text{Mpc}$ for DES, BOSS, and *Planck* shown in Fig. 1. The issue with σ_8 is then that its marginalized value corresponds to a weighted average of σ_R on a range of scales
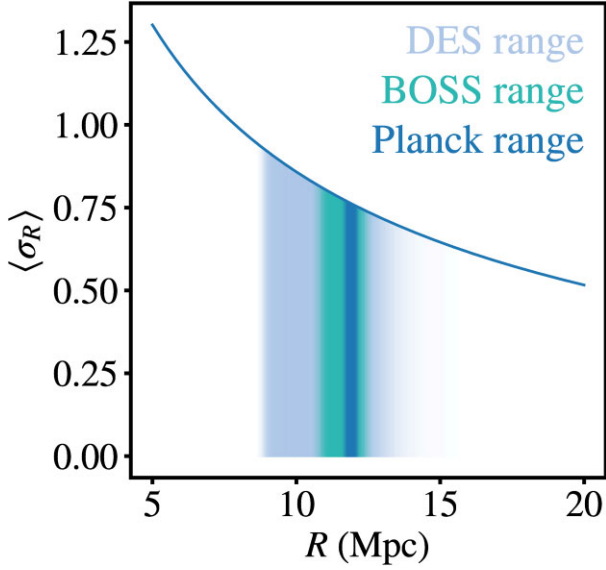
Figure 2. The change of the value of standard deviation of linear matter fluctuations σ_R measured in a sphere of physical radius R in Mpc in *Planck* ΛCDM Universe. The shaded areas indicate the ranges that $(8/h)\,\mathrm{Mpc}$ correspond to for BOSS, DES, and *Planck* based on the posteriors in Fig. 1. When R is defined in $h^{-1}\mathrm{Mpc}$, as is the case for σ_8, the value measured is, in fact, a weighted average of σ_R over a range of R.

Table 1. Priors used in our analysis. U indicates a flat uniform prior within the specified range. The priors on the cosmological and clustering nuisance parameters match those of Tröster et al. (2020) with the exception of n_s, for which the allowed range is widened. The priors on the nuisance parameters of weak lensing data sets match those of Abbott et al. (2018).

Parameter	Prior
Cosmological parameters	
$\Omega_b h^2$	$U(0.019, 0.026)$
$\Omega_c h^2$	$U(0.01, 0.2)$
$100\theta_{MC}$	$U(0.5, 10.0)$
τ	$U(0.01, 0.8)$
$\ln(10^{10} A_s)$	$U(1.5, 4.0)$
n_s	$U(0.5, 1.5)$
Clustering nuisance parameters	
b_1	$U(0.5, 9.0)$
b_2	$U(-4.0, 8.0)$
a_{vir}	$U(0.0, 12.0)$
σ_{err}(eBOSSonly)	$U(0.01, 6.0)$

that is different for each data set. A further complication is that the value of h also has an impact on the amplitude of σ_R. As discussed in Sánchez (2020), these issues can be avoided by considering the variance of the density field on a reference scale in Mpc such as σ_{12}, which is equivalent to σ_8 but is defined on a physical scale of $12\,\mathrm{Mpc}$. We therefore opt to focus on σ_{12} and quantities that carry no explicit dependence on the Hubble constant h in order to enable us to appropriately combine and compare the constraints from our data sets.

We obtain the posterior distribution of all these parameters by performing Markov chain Monte Carlo sampling with COSMOMC (Lewis & Bridle 2002), which uses CAMB to calculate the linear-theory matter power spectra (Lewis et al. 2000), adapted to compute the theoretical model of our anisotropic clustering measurements described in Section 2.2. COSMOMC uses as basis parameters the set

$$\boldsymbol{\theta}_{\mathrm{base}} = (\omega_b, \omega_c, \Theta_{MC}, A_s, n_s), \qquad (20)$$

where Θ_{MC} is defined by a factor 100 times the approximate angular size of the sound horizon at recombination. With the exception of the physical baryon density, we assign flat uninformative priors to all the parameters of equation (20) as was done in Tröster et al. (2020). Our prior for ω_b has to be restrictive, as our clustering measurements cannot constrain this parameter by themselves. Nevertheless, it is chosen to be approximately 25 times wider than the constraints on this parameter derived from *Planck* data alone (Planck Collaboration VI 2020). Even though we do not sample the Hubble parameter h, we still need to specify the values allowed – our chosen range $0.5 < h < 0.9$ is wider than that of the KiDS-450 analysis of Hildebrandt et al. (2016) and comparable to the one used in the DES-YR1 fiducial analysis of Abbott et al. (2018). Joudaki et al. (2016) showed that the prior on h has no impact on the significance of the σ_8 tension. We list all the priors used in this analysis in Table 1.

As discussed by Sanchez et al. (2021), the effect of all evolution parameters on the linear matter power spectrum is degenerate: for a

given set of shape parameters, the linear power spectra of all possible combinations of evolution parameters that lead to the same value of $\sigma_{12}(z)$ are identical. This behaviour is inherited by the non-linear matter power spectrum predicted by RESPRESSO, which depends exclusively on $P_L(k)$. However, the full model of $P(k, \mu)$ does not follow this simple degeneracy due to the effect of bias, RSD and AP distortions. Of the parameters listed in equation (17), ω_b, ω_c, and n_s are shape parameters, while ω_{DE} and A_s are purely evolution parameters. Other quantities such as h or Ω_i represent a mixture of both shape and evolution parameters.

Present-day CMB measurements can constrain the values of most shape parameters with high accuracy, with posterior distributions that are well described by a multivariate Gaussian, independently of the evolution parameters being explored. On the other hand, clustering measurements on their own provide only weak constraints on the values of the shape parameters. However, if the shape parameters are fixed, clustering data can provide precise measurements of the evolution parameters. To test the impact of the additional information on the shape of the linear power spectrum, along with the priors described above, we use another set of priors to explore the constraints on the evolution parameters. For these runs, we impose Gaussian priors on the cosmological parameters that control the shape of the linear power spectrum – ω_b, ω_c, and n_s. We derived the covariance matrix and mean values for these priors from our *Planck*-only posterior distributions. We refer to these constraints as the '*Planck* shape' case.

2.5 Model validation

As we are using an updated prescription for the modelling of both the non-linear matter power spectrum and galaxy bias compared to the previous work of Tröster et al. (2020), we want to assess if it can recover unbiased cosmological parameter estimates, using mock data based on numerical simulations as a testing ground. We do so by applying our model to the mocks that were used for model validation in the original analyses: the MINERVA simulations (Grieb et al. 2016; Lippich et al. 2019) for a BOSS-like sample and OUTERRIM (Heitmann et al. 2019) for an eBOSS-like data set.

MINERVA mocks are produced from a set of 300 N-body simulations with 1000^3 particles and a box size of $L = 1.5\,h^{-1}\,\mathrm{Gpc}$. The snapshots at $z = 0.31$ and $z = 0.57$ were used to create halo catalogues
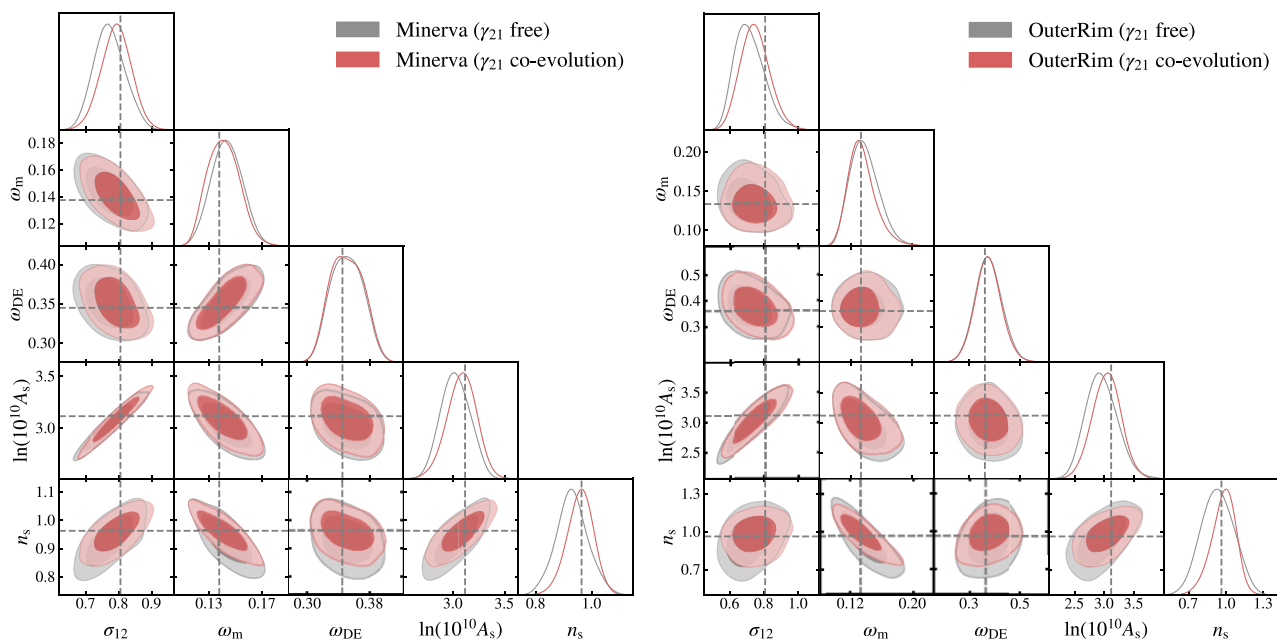
Figure 3. Flat ΛCDM constraints derived from mean measurements of MINERVA (left) and OUTERRIM (right) HOD samples using the model described in Section 2.2 while freely varying the non-local bias parameters γ_{21} (grey contours) and when its value is fixed using the co-evolution relation of equation (9) (red). The dashed lines mark the true input parameter values. Both cases recover the input cosmology well but the co-evolution relations yield slightly more accurate and precise constraints.

with a minimum halo mass of $M_{\min} = 2.67 \times 10^{12} h^{-1} M_\odot$, which were populated with synthetic galaxies using the halo occupation distribution (HOD) model by Zheng, Coil & Zehavi (2007) with parameters designed to reproduce the clustering properties of the LOWZ and CMASS galaxy samples from BOSS.

The OUTERRIM (Heitmann et al. 2019) simulation uses $10\,240^3$ dark matter particles to trace the dark matter density field in a $L = 3\,h^{-1}$ Gpc size box. We use a set of 100 mock catalogues constructed from the snapshot at $z = 1.433$, which was populated using an HOD model matching the clustering of the eBOSS QSO sample and tested extensively in the mock challenge (labelled as HOD0 in Smith et al. 2020). These realizations include catastrophic redshift failures at a rate of 1.5 per cent, which corresponds to that of the eBOSS quasars.

We measured the mean clustering wedges of the samples from MINERVA and the Legendre multipoles from OUTERRIM with the same binning and range of scales as those of the real data from BOSS and eBOSS and computed their corresponding theoretical covariance matrices using the Gaussian recipe of Grieb et al. (2016). We analysed these measurements using identical nuisance and cosmological parameter priors as for our final results and tested the validity of the model described in Section 2.2 with and without the assumption of the co-evolution relation for γ_{21} of equation (9). We performed a joint fit of the two BOSS-like samples from MINERVA while the OUTERRIM measurements, which correspond to a different cosmology, were analysed separately. Fig. 3 shows the posterior distributions recovered from these measurements, which are in excellent agreement with the true input cosmology for all cases (shown by the dashed lines). Nevertheless, we find that setting the value of γ_{21} according to equation (9) recovers the true parameter values more accurately for both samples and results in tighter constraints than when it is freely varied. We therefore adopt this approach in the analysis of the clustering measurements from BOSS and eBOSS.

3 RESULTS

Our main results come from the combination of the full shape analyses of the BOSS galaxy clustering wedges and eBOSS QSO Legendre multipoles described in Section 2.1. We also present combined late-Universe constraints obtained from the joint analysis of these clustering measurements with the 3 × 2pt data set from DES Y1. For comparison, in Appendix A, we present the constraints obtained using instead the cosmic shear measurements from KiDS-450, which lead to similar results. As we find a good agreement between BOSS + eBOSS + DES and *Planck*, we also present the parameter constraints obtained from the combination of all four data sets. These constraints are summarized in Table 2 and are discussed in Sections 3.1–3.3.

3.1 Clustering constraints

Here, we present the main result of our work – the combined flat ΛCDM constraints from the anisotropic clustering measurements from BOSS and eBOSS. Fig. 4 shows the posterior distributions for BOSS and eBOSS separately (light blue and orange contours, respectively) as well as their combined constraints (green contours) for two sub-sets of cosmological parameters. For comparison, we also show the *Planck*-only constraints in dark blue. The panels on the left show the results on the more traditional parameter set of σ_8, Ω_m, and H_0 whereas the ones on the right correspond to the alternative basis discussed in Section 2.4 of σ_{12}, ω_m, and ω_{DE}.

Regardless of the parameter space considered, we find all of our data sets to be in good agreement with each other. The largest deviation between the joint BOSS + eBOSS constraints and those recovered from *Planck* can be observed in the matter density Ω_m, which displays a difference at the 1.7σ level. Nevertheless, this deviation does not indicate a similarly significant disagreement in the physical matter density preferred by these probes, as the

Table 2. Marginalized posterior constraints (mean values with 68 per cent confidence interval) derived from the full shape analysis of BOSS + eBOSS clustering measurements on their own, as well as in combination with the 3 × 2pt measurements from DES Y1 and the CMB data from *Planck*. We present two sets of constraints: our main results derived with wide priors, as listed in Table 1, and the '*Planck* shape' constraints obtained by imposing narrow Gaussian priors on the cosmological parameters controlling the shape of the linear power spectrum: the physical baryon density ω_b, the physical cold dark matter density ω_c, and the spectral index n_s, as discussed in Section 2.4.

| | Wide priors | | | Gaussian priors on ω_b, ω_c, n_s | |
| | | BOSS + eBOSS | BOSS + eBOSS + | | BOSS + eBOSS |
Parameter	BOSS + eBOSS	+ DES	DES + *Planck*	BOSS + eBOSS	+ DES
σ_{12}	0.805 ± 0.049	$0.795^{+0.032}_{-0.037}$	0.7890 ± 0.0078	0.785 ± 0.039	0.766 ± 0.019
ω_m	0.134 ± 0.011	0.131 ± 0.011	0.14090 ± 0.00085	0.1426 ± 0.0013	0.1423 ± 0.0012
ω_{DE}	0.328 ± 0.020	0.327 ± 0.020	0.3268 ± 0.0064	$0.327^{+0.011}_{-0.013}$	0.335 ± 0.011
$\ln 10^{10} A_s$	3.13 ± 0.15	3.14 ± 0.13	3.041 ± 0.016	3.011 ± 0.099	2.976 ± 0.054
n_s	1.009 ± 0.048	1.001 ± 0.047	0.9700 ± 0.0038	0.9660 ± 0.0044	0.9665 ± 0.0043
σ_8	0.815 ± 0.044	0.803 ± 0.028	0.8029 ± 0.0066	0.800 ± 0.039	0.785 ± 0.021
Ω_m	$0.290^{+0.012}_{-0.014}$	$0.286^{+0.011}_{-0.013}$	0.3014 ± 0.0053	0.3037 ± 0.0081	0.2985 ± 0.0072
h	0.679 ± 0.021	0.677 ± 0.021	0.6838 ± 0.0041	$0.6855^{+0.0084}_{-0.0094}$	0.6905 ± 0.0083
S_8	0.801 ± 0.043	0.783 ± 0.020	0.805 ± 0.011	0.805 ± 0.042	0.783 ± 0.019
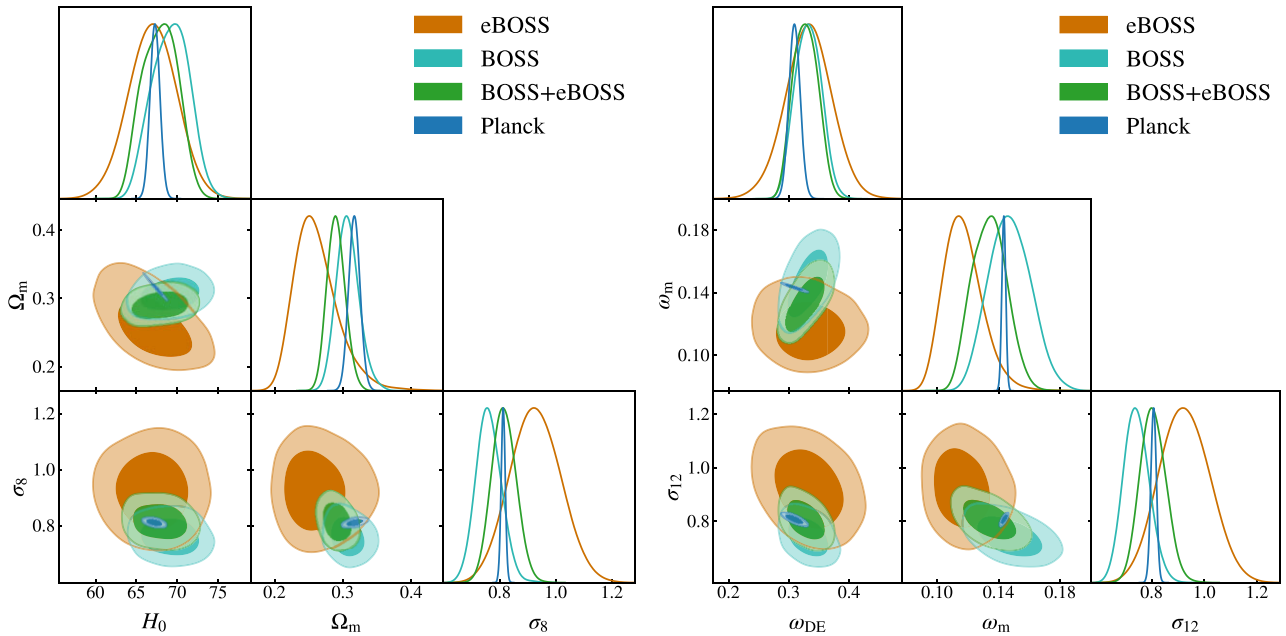
Figure 4. Marginalized posterior contours in the 'traditional' and *h*-independent parameter spaces from the Legendre multipoles of eBOSS QSO sample (orange) and the clustering wedges of BOSS DR12 galaxies (light blue) for a flat ΛCDM model. The joint constraints are shown in green, with *Planck* in dark blue for comparison.

value of ω_m recovered by our clustering constraints matches that of *Planck* within 0.8σ. This suggests that the differences seen in Ω_m are related to the posterior distributions on *h* recovered from these data sets. Indeed, looking at our *h*-independent parameter space, we see that the marginalized constraint of the physical dark energy density also differs from the value preferred by *Planck* by 0.8σ, with clustering measurements preferring slightly higher ω_{DE}, which translates into a higher value for H_0 and a lower Ω_m.

Tröster et al. (2020) found that the clustering measurements from BOSS wedges prefer a 2.1σ lower value of σ_8 as compared to *Planck*. Here, we confirm the low preference, albeit with much lower significance due to the differences in the modelling of the power

spectrum, for both σ_8 and σ_{12} (consistent with *Planck* at the 1.1σ and 1.3σ level, respectively). The increased consistency between these results is mainly due to the tighter constraints enabled by the use of the co-evolution relation of equation (9), which restricts the allowed region of the parameter space to higher values of σ_8 and σ_{12}, as can be seen in Fig. 3. The constraints on σ_8 and σ_{12} recovered from eBOSS are at similar levels of agreement with *Planck*; however, the values recovered are 1.3σ and 1.2σ *higher* than the CMB results. This is also consistent with the most recent analysis by Hou et al. (2021) and Neveux et al. (2020), who found the inferred growth rate $f\sigma_8$ to be $\sim 2\sigma$ higher than the ΛCDM model with the best-fitting *Planck* parameters. The combination of the clustering measurements from BOSS and eBOSS is therefore in an overall excellent agreement
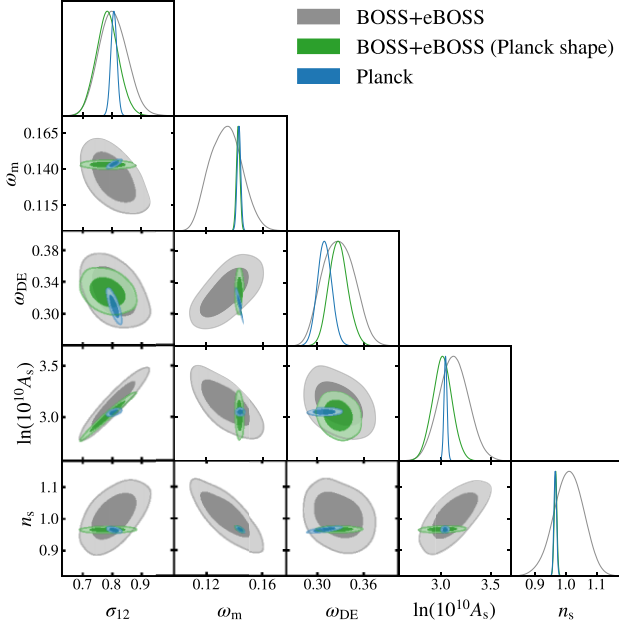
Figure 5. When an informative prior is imposed on BOSS + eBOSS for the shape parameters ω_b, ω_c, and n_s so as to match the power spectrum shape obtained by *Planck*, the recovered constraints (in green) on the evolution parameters are in a good agreement with *Planck* (dark blue) with a slightly more significant deviation in ω_{DE} only: BOSS + eBOSS prefer a $\sim 1.2\sigma$ higher value of ω_{DE} than *Planck*.

with *Planck* – with differences at the level of 0.05σ for σ_8 and 0.04σ for σ_{12}.

As discussed in Section 2.4, the shape parameters ω_b, ω_c, and n_s are all tightly constrained by *Planck* with posterior distributions that are in complete agreement with those inferred from the other cosmological probes considered here. We can therefore study the improvement in the constraints on the evolution parameters ω_{DE} and A_s that are obtained from the LSS probes when the shape of the power spectrum is constrained to match that of *Planck*'s cosmology. As described in Section 2.4, we achieve this by adding an informative Gaussian prior on the shape parameters based on our *Planck* runs and repeating our analysis with an otherwise identical set-up.

The results of this exercise are shown in Fig. 5. As the two data sets were already in a good agreement across the parameter space, including the shape parameters, imposing additional priors simply adds constraining power on the degenerate evolution parameters, most notably ω_{DE} (degenerate with ω_m), which is recovered to be slightly higher than the *Planck* value to compensate the slight shifts in σ_{12} and $\ln(10^{10}A_s)$ to lower values.

3.2 Consistency with *Planck*

When looking at marginalized posteriors we are limited by our selection of the parameter space as well as the associated projection effects and, while we can use the standard deviation to quantify agreement on a particular parameter value, this becomes inappropriate when larger parameter spaces are considered. We therefore wish to further explicitly quantify the agreement between eBOSS + BOSS and *Planck* using a tension metric, as has become standard in cosmological analyses.

First, we want to establish agreement over the whole parameter space considered. In order to do this, we use the suspiciousness tension metric, S, introduced by Handley & Lemos 2019. The main

advantages of using suspiciousness include the fact that it measures the agreement between two data sets across the entire parameter space, similarly to the Bayes factor R. However, unlike R, the suspiciousness is by construction insensitive to prior widths, as long as the posterior is not prior-limited. Given two data sets, A and B, the suspiciousness quantifies the mismatch between them by comparing the relative gain in confidence in data set A when data set B is added (as measured by R) with the unlikeliness of the two data sets ever matching as measured by the information ratio I, that is

$$\ln S = \ln R - \ln I. \tag{21}$$

Following the method described in Heymans et al. (2021), we redefine $\ln R$ and $\ln I$ in terms of the expectation values of the log-likelihoods $\langle \ln \mathcal{L} \rangle$ and evidences Z. The evidences, however, cancel out and we are able to calculate S from the expectation values only:

$$\ln S = \langle \ln \mathcal{L}_{A+B} \rangle_{P_{A+B}} - \langle \ln \mathcal{L}_A \rangle_{P_A} - \langle \ln \mathcal{L}_B \rangle_{P_B} . \tag{22}$$

The value of S can then be interpreted using the fact that, for Gaussian posteriors, the difference $d - 2\ln S$, where d is the Bayesian model dimensionality, is χ_d^2 distributed. We calculate d for each of the data sets separately, d_A and d_B, and their combination, d_{A+B}, as described in Handley & Lemos (2019) and combine the results as $d = d_A + d_B - d_{A+B}$.

Applying this procedure to eBOSS + BOSS and *Planck*, we find $\ln S = 0.41 \pm 0.07$ with a Bayesian dimensionality of $d = 4.5 \pm 0.4$, which correctly indicates that there are approximately five cosmological parameters shared between the two data sets. This can then be related to a p-value of $p = 0.52 \pm 0.02$ or a tension of $0.64 \pm 0.03\sigma$, which is consistent with the $0.76 \pm 0.05\sigma$ tension between *Planck* and BOSS alone found by Tröster et al. (2020) and indicates a good agreement between these data sets.

In addition to the suspiciousness, we want to use a tension metric that allows for a greater control to focus only on a selected subset of parameters. For this purpose, we use the updated difference-in-mean statistic, $\mathcal{Q}_{UDM}$, as described in Raveri & Hu (2019) and implemented in TENSIOMETER[1] (Lemos et al. 2021). This statistic extends the simple difference in means, where the difference in mean parameter values $\hat{\theta}$ measured by two data sets is weighted by their covariance $\mathbf{C}$. The 'update' in UDM refers to the fact that instead of comparing data set A with data set B, we consider the updated information in the combination A + B with respect to A by means of

$$\mathcal{Q}_{UDM} = \left(\hat{\theta}_{A+B} - \hat{\theta}_A \right)^t \left(\mathbf{C}_A - \mathbf{C}_{A+B} \right)^{-1} \left(\hat{\theta}_{A+B} - \hat{\theta}_A \right) . \tag{23}$$

This has the advantage of the posterior of A + B being more Gaussian than that of B alone. For Gaussian distributed parameters, $\mathcal{Q}_{UDM}$ is chi-square distributed with a number of degrees of freedom given by the rank of $(\mathbf{C}_A - \mathbf{C}_{A+B})$. The calculation of $\mathcal{Q}_{UDM}$ may be performed by finding the Karhunen–Loéve modes of the covariances and re-expressing the cosmological parameters in this basis. This transformation allows us to reduce the sampling noise by imposing a limit to the eigenvalues of the modes that are considered and in this way cutting out those that are dominated by noise (which represent the directions in which adding B does not improve the constraints with respect to A). The number of remaining modes correspond to the degrees of freedom with which $\mathcal{Q}_{UDM}$ is distributed. For our tension calculations, we therefore only select the modes α whose eigenvalues λ_α satisfy :

$$0.05 < \lambda_\alpha - 1 < 100. \tag{24}$$

[1] https://github.com/mraveri/tensiometer
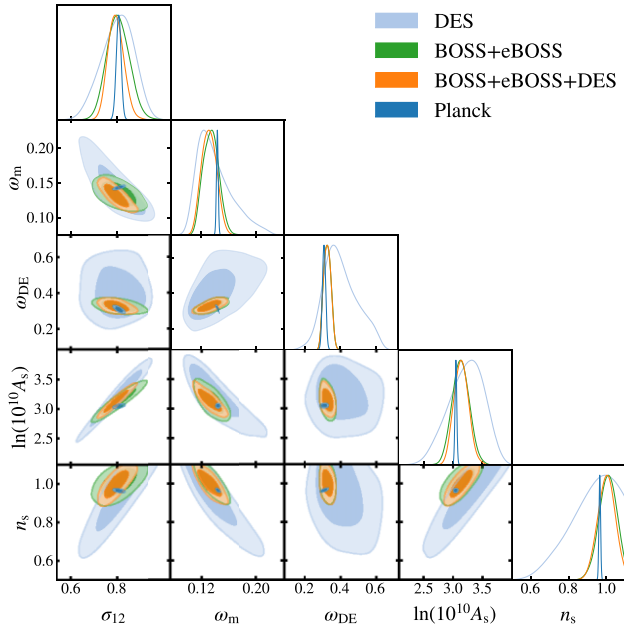
Figure 6. In orange – 'low-redshift' constraints for flat ΛCDM obtained from combining BOSS + eBOSS clustering (green) with DES 3 × 2pt (light blue) and compared with *Planck* (dark blue). While we obtain a good consistency overall, we note the slight discrepancy between the low-redshift probes and *Planck* contours in $\log(10^{10}A_s)$–σ_{12} and ω_m–σ_{12} projections, reminiscent of the tension seen in σ_8–Ω_m plane.

This corresponds to requiring that a mode of the base data set is updated by at least 5 per cent. We subsequently find that there are 2 modes being constrained when *Planck* is updated by both probe combinations considered in this work (BOSS + eBOSS and BOSS + eBOSS + DES).

For BOSS + eBOSS, we get $\mathcal{Q}_{\mathrm{UDM}} = 2.0$ for the full parameter space, resulting in a 'tension' with *Planck* of 0.90σ – only slightly higher than what S suggests.

3.3 Joint analysis with DES data

Following Tröster et al. (2020), we want to further investigate the constraints from multiple low-redshift probes together by adding a weak lensing data set – in this case, the 3 × 2pt measurements from DES Y1. Tröster et al. (2020) used the suspiciousness statistic and showed that the combination of BOSS clustering and KiDS-450 shear measurements are in ∼ 2σ tension with *Planck*. The most recent KiDS-1000 3 × 2pt analysis (Heymans et al. 2021), where the BOSS galaxy sample was used for galaxy clustering and galaxy–galaxy lensing measurements, also found a similar level of tension when the entire parameter space is considered. As DES Y1 measurements have no overlap with either BOSS or eBOSS, we can treat these data sets as independent and easily combine them to test whether we also find a similar trend.

The resulting constraints are presented in Fig. 6. We confirm that DES is in good agreement with eBOSS + BOSS (with $\ln S = -1.08 \pm 0.05$, which corresponds to a $1.3 \pm 0.08\sigma$ tension) and it is therefore safe to combine them. The addition of DES data to the analysis provides only slightly tighter constraints with respect to eBOSS + BOSS, with the greatest improvement in σ_{12}, and an overall good agreement with *Planck*.

Nevertheless, it is worth noting that, when considering the 2D posterior projections, there are two parameter combinations in

particular for which the 1σ contours of DES + BOSS + eBOSS and *Planck* do not overlap. The slight discrepancy we observe in the ω_m–σ_{12} plane is reminiscent of the 'σ_8 tension' seen in Ω_m–σ_8 and is larger than the discrepancy displayed by either of the probes individually. In addition to that, we also see a similarly slight disagreement in the $\ln(10^{10}A_s)$–σ_{12} plane. The projection of A_s with σ_{12} (as opposed to σ_8) allows us to recover the tight degeneracy between the two parameters that exposes how, for a given present-day clustering amplitude, low-redshift probes prefer a higher initial power spectrum amplitude.

We find that adding the DES Y1 3 × 2pt measurements worsens the agreement with *Planck* with respect to the results obtained from the combination of BOSS and eBOSS alone. We obtain a suspiciousness of $\ln S = -1.86 \pm 0.04$, corresponding to a tension of $1.54 \pm 0.08\sigma$. When considering the UDM statistic across the entire shared parameter space, we find $\mathcal{Q}_{\mathrm{UDM}} = 6.3$ distributed with 2 degrees of freedom, which translates into a tension at the 1.9σ level. As for the case of the clustering-only constraints, $\mathcal{Q}_{\mathrm{UDM}}$ indicates a greater level of tension than S.

Lemos et al. (2021) found that the DES Y1 3 × 2pt measurements alone are in a 2.3σ tension with *Planck*, as measured by $\mathcal{Q}_{\mathrm{UDM}}$. This increases to $2.4 \pm 0.02\sigma$ when using the suspiciousness statistic. These levels of tension are comparable with what we find from the full combination of low-redshift probes. The tension between *Planck* and weak lensing data sets is usually interpreted as a reflection of tension in the parameter combination $S_8 = \sigma_8(\Omega_m/0.3)^{0.5}$, that is taken to describe the 'lensing strength'. The S_8 value that we recover from the joint low-redshift probes is also about 2σ lower than the *Planck* constraint (see Table 2). Nevertheless, as we see in Fig. 6, there is a comparable discrepancy in $\log(10^{10}A_s)$–σ_{12} plane. We can use $\mathcal{Q}_{\mathrm{UDM}}$ in order to quantify and compare the level of tension present in these 2D projections by calculating it for a subset of shared parameter space. We find that the amount of tension in both Ω_m–σ_8 and its h-independent equivalent is ∼2.0σ, whereas $\log(10^{10}A_s)$–σ_{12} displays a slightly higher tension of 2.5σ.

We also repeated our fitting procedure with an additional Gaussian prior on the parameters controlling the shape of the power spectrum to be consistent with *Planck*, as described in Section 2.4. The resulting posteriors are shown in Fig. 7. We observe the same general trends as from the analysis of our clustering data alone discussed in Section 3.1. However, the prior on the shape parameters leads to larger shifts in the evolution parameters. This is expected, as DES data on their own cannot constrain the shape parameters well. Adding the informative priors breaks the denegeracies between shape and evolution parameters and increases the constraining power significantly. This, in turn, exposes any discrepancies in the evolution parameters. The values of σ_{12} and $\ln(10^{10}A_s)$ preferred by our low-redshift probes when an informative prior is imposed are, respectively, 1.89σ and 1.22σ lower than the corresponding *Planck* values. Meanwhile, the recovered value for ω_{DE} is 1.73σ higher.

4 DISCUSSION

The flat ΛCDM constraints from the low-redshift probes presented in Section 3 show a consistent picture. Updating the power spectrum model and supplementing the clustering measurements with eBOSS data brings the joint BOSS + eBOSS constraints to a better agreement with *Planck* than the BOSS-only results from Tröster et al. (2020). These constraints are not significantly modified when these data are combined with DES, resulting in a good overall consistency with *Plank* across the entire parameter space, as indicated by both S and $\mathcal{Q}_{\mathrm{UDM}}$.
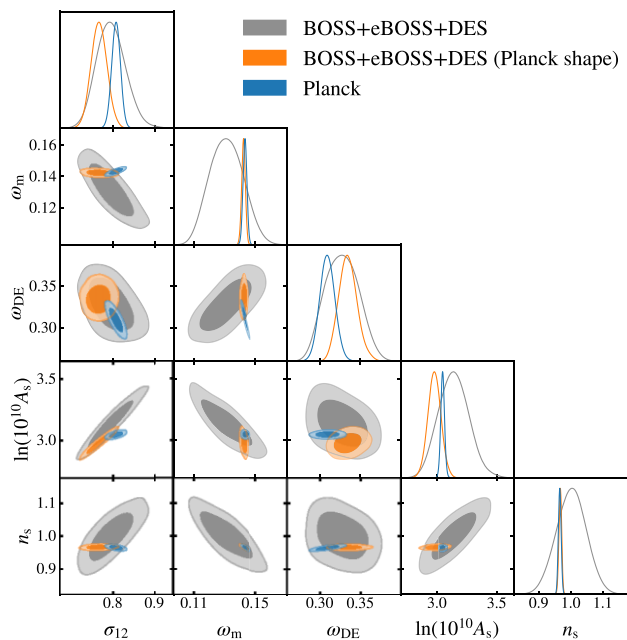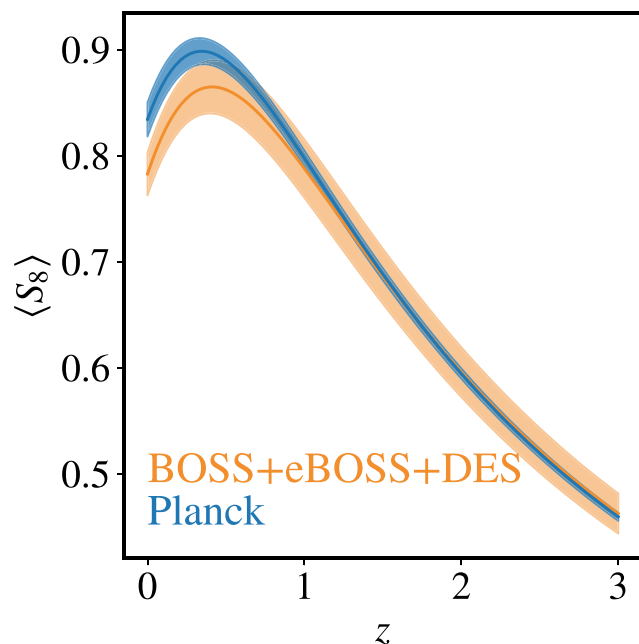
Figure 7. Constraints on flat ΛCDM models from the full combination of low-redshift probes (DES + BOSS + eBOSS) obtained after imposing a *Planck* prior on shape parameters n_s, ω_b, and ω_c (orange contours). The constraints from the original uninformative prior analysis (grey contours) and *Planck* (dark blue contours) are shown for comparison. The results show similar trends as in the case of BOSS + eBOSS. There is a shift to higher values of ω_{DE} that leads to a lower power spectrum amplitude today, σ_{12}, and, to a lesser extent, a lower $\log(10^{10}A_s)$.

Figure 8. Comparison of the inferred mean value for $S_8(z)$ (solid lines) and their corresponding 68 per cent confidence level (shaded area) corresponding to the combination of BOSS + eBOSS + DES (orange) and *Planck* (blue).

Nevertheless, when considering specific 2D projections we still see intriguing differences, mainly driven by the lensing data. Although the constraints in the σ_{12}–ω_m plane obtained using BOSS + eBOSS and DES data separately do not show the discrepancy with *Planck* that characterizes the results in their h-dependent counterparts of σ_8 and Ω_m, the full combination of low-redshift probes tightens the degeneracy between these parameters and leads to constraints that are just outside the region of the parameter space preferred by *Planck*.

We also see differences in the $\log(10^{10}A_s)$–σ_{12} plane between DES and *Planck*, which are inherited by the full combination of low-redshift data sets. The tight relation between these parameters, which is not seen when using σ_8, illustrates the closer link between σ_{12} and the overall amplitude of density fluctuations obtained by eliminating the ambiguity caused by the dependence on h. For a given value of σ_{12}, *Planck* measurements prefer a lower initial amplitude of density fluctuations than DES, suggesting a discrepancy in the total growth of structures predicted by these two data sets.

Within the context of a ΛCDM model, the key parameter controlling the growth of structure at low redshift is the physical dark energy density. Indeed, as can be seen in Fig. 6, the posterior distribution of ω_{DE} recovered from DES extends to significantly higher values than the one obtained using *Planck* CMB measurements. The tendency of the low-redshift data to prefer a higher value of ω_{DE} than that of *Planck* can be seen more clearly in the results obtained after imposing a prior on the shape parameters shown in Fig. 7. In this case, we find $\omega_{DE} = 0.335 \pm 0.011$ using BOSS + eBOSS + DES while *Planck* data lead to $\omega_{DE} = 0.3093 \pm 0.0093$. A higher value of ω_{DE} corresponds also to a higher value of h. Therefore, this difference is also interesting in the context of the Hubble tension, as many of the

proposed solutions to this issue focus on modifying the dark energy component.

The analysis of the consistency between low- and high-redshift data has been focused on the comparison of constraints on S_8, which depends on the present-day value of σ_8. Fig. 8 shows the redshift evolution of $S_8(z)$ predicted by *Planck* and the combination of all low-redshift data sets. These curves are consistent at high redshift during matter domination and start to diverge at $z < 1$ to reach a difference at the 2σ level at $z = 0$. However, as this redshift is not probed by any LSS data set, the value of $S_8(z = 0)$ is an extrapolation based on the assumption of a ΛCDM background evolution. Extending this extrapolation to $a > 1$, the difference between the two cosmologies continues to increase and becomes even more significant. Therefore, quoting the statistical significance of any discrepancy in the recovered values of $S_8(z = 0)$ might not be the best characterization of the difference in the cosmological information content of these measurements.

As discussed before, DES and *Planck* data appear to prefer different evolutions for the growth of cosmic structure, which in a ΛCDM universe depends on ω_m and ω_{DE}. As the former is exquisitely constrained by *Planck* for general parameter spaces, the latter is perhaps the most interesting parameter to consider. As ω_{DE} is constant in redshift for a ΛCDM universe, the deviations in the value of this parameter recovered from different data sets could be used as an indication of their consistency within the standard cosmological model.

5 CONCLUSIONS

We obtained constraints on the parameters of the standard ΛCDM model from the joint analysis of anisotropic clustering measurements in configuration space from BOSS and eBOSS. In particular, we used the information of the full shape of the clustering wedges of the final BOSS galaxy samples obtained by Sánchez et al. (2017) and the legendre multipoles of the eBOSS DR16 QSO catalogue

of Hou et al. (2021). We updated the recipes to describe the non-linear matter power spectrum and the non-local bias parameters with respect to those used in the BOSS-only analyses of Sánchez et al. (2017) and Tröster et al. (2020). We directly compared our theoretical predictions for different cosmologies against the BOSS and eBOSS clustering measurements, without the commonly used RSD and BAO summary statistics. We focus on cosmological parameters that can be classified either as shape or evolution parameters (Sanchez et al. 2021), such as the physical matter and dark energy densities, instead of other commonly used quantities such as Ω_m and Ω_{DE} that depend on the value of h. Our constraints from the combination of BOSS + eBOSS represent improvements ranging from 20 to 25 per cent with respect to those of Tröster et al. (2020) and are in excellent agreement with *Planck*, with the suspiciousness and updated difference in means tension metrics indicating agreement at the level of 0.64σ and 0.90σ, respectively.

We combined the clustering data from BOSS and eBOSS with the 3×2pt correlation function measurements from DES Y1 to obtain joint low-redshift cosmological constraints that are also consistent with the ΛCDM *Planck* results, albeit with larger deviations (1.54σ and 2.00σ differences as inferred from S and $\mathcal{Q}_{UDM}$, respectively). We do see interesting discrepancies in certain parameter combinations at the level of 2σ or more, such as the $\Omega_m-\sigma_8$ and $\omega_m-\sigma_{12}$ planes, and, more significantly, in the $\log(10^{10}A_s)-\sigma_{12}$ projection. For a given value of σ_{12}, low-redshift probes (mostly driven by DES) prefer a higher amplitude of primordial density fluctuations than *Planck*, indicating differences in the total growth of structure predicted by these data sets.

We further tested the impact of imposing a Gaussian prior on ω_b, ω_c, and n_s representing the constraints on these shape parameters recovered from *Planck* data. Such prior leads to a significant improvement in the constraints on the evolution parameters, such as ω_{DE} and A_s. In this case, we find that the full combination of low-redshift data sets prefers a value of the physical dark energy density ω_{DE} that is 1.7σ higher than that preferred by *Planck*. This discrepancy, which is also related to the amount of structure growth preferred by these data sets, offers an interesting link with the H_0 tension, as it points to a higher value of h being preferred by the low-redshift data.

The advent of new large, high-quality data sets such as the Dark Energy Spectroscopic Instrument (DESI; DESI Collaboration 2016), the ESA space mission *Euclid* (Laureijs et al. 2011), and the Legacy Survey of Space and Time at the Rubin Observatory (Ivezić et al. 2019), will allow us to combine multiple probes and significantly tighten our cosmological constraints. The discussion of the consistency between different data sets has so far been centred on the comparison of constraints on $S_8(z = 0)$. As we move on to the analysis of Stage IV data sets, it would be beneficial to shift our focus from best constrained parameter combinations within a ΛCDM scenario to quantities that more closely represent the cosmological information content of those data, or that have a more direct physical interpretation.

DATA AVAILABILITY

The clustering measurements from BOSS and eBOSS used in this analysis are publicly available via the SDSS Science Archive Server (https://sas.sdss.org/).

REFERENCES

Abbott T. M. C. et al., 2018, Phys. Rev., D98, 043526
Ahumada R. et al., 2020, ApJS, 249, 3
Alam S. et al., 2015, ApJS, 219, 12
Alam S. et al., 2017, MNRAS, 470, 2617
Alam S. et al., 2021, Phys. Rev. D, 103, 083533
Alcock C., Paczyński B., 1979, Nature, 281, 358
Anderson L. et al., 2012, MNRAS, 427, 3435
Bautista J. E. et al., 2021, MNRAS, 500, 736
Begeman K., Belikov A., Boxhoorn D., Valentijn E., 2012, Exp. Astron., 35, 1
Bel J., Pezzotta A., Carbone C., Sefusatti E., Guzzo L., 2019, A&A, 622, A109
Blanton M. R. et al., 2017, AJ, 154, 28
Bridle S., King L., 2007, New J. Phys., 9, 444
Brieden S., Gil-Marín H., Verde L., 2021, JCAP, 2021, 054
Catelan P., Lucchin F., Matarrese S., Porciani C., 1998, MNRAS, 297, 692
Catelan P., Porciani C., Kamionkowski M., 2000, MNRAS, 318, L39
Chan K. C., Scoccimarro R., Sheth R. K., 2012, Phys. Rev. D, 85, 083509
Chen S.-F., Vlah Z., White M., 2022, JCAP, 2022, 008

Cole S. et al., 2005, MNRAS, 362, 505
d'Amico G., Gleyzes J., Kokron N., Markovic K., Senatore L., Zhang P., Beutler F., Gil-Marín H., 2020, J. Cosmol. Astropart. Phys., 2020, 005
Dawson K. S. et al., 2013, AJ, 145, 10
Dawson K. S. et al., 2016, AJ, 151, 44
de Jong J. T. A. et al., 2017, A&A, 604, A134
de Mattia A. et al., 2021, MNRAS, 501, 5616
DES Collaboration, 2021, Phys. Rev. D, 105, 023520
DESI Collaboration, 2016, preprint (arXiv:1611.00036)
Eggemeier A., Scoccimarro R., Smith R. E., 2019, Phys. Rev. D, 99, 123514
Eggemeier A., Scoccimarro R., Crocce M., Pezzotta A., Sánchez A. G., 2020, Phys. Rev. D, 102, 103530
Eggemeier A., Scoccimarro R., Smith R. E., Crocce M., Pezzotta A., Sánchez A. G., 2021, Phys. Rev. D, 103, 123550
Eisenstein D. J. et al., 2005, ApJ, 633, 560
Eisenstein D. J. et al., 2011, AJ, 142, 72
Erben T. et al., 2013, MNRAS, 433, 2545
Fenech Conti I., Herbonnet R., Hoekstra H., Merten J., Miller L., Viola M., 2017, MNRAS, 467, 1627
Fry J. N., 1996, ApJ, 461, L65
Gil-Marín H. et al., 2020, MNRAS, 498, 2492
Grieb J. N., Sánchez A. G., Salazar-Albornoz S., Dalla Vecchia C., 2016, MNRAS, 457, 1577
Gunn J. E. et al., 2006, AJ, 131, 2332
Handley W., Lemos P., 2019, Phys. Rev. D, 100, 043504
Hartlap J., Simon P., Schneider P., 2007, A&A, 464, 399
Heitmann K. et al., 2019, ApJS, 245, 16
Heymans C. et al., 2021, A&A, 646, A140
Hikage C. et al., 2019, PASJ, 71, 43
Hildebrandt H. et al., 2016, MNRAS, 465, 1454
Hildebrandt H. et al., 2020, A&A, 633, A69
Hill J. C., McDonough E., Toomey M. W., Alexander S., 2020, Phys. Rev. D, 102, 043507
Hinshaw G. et al., 2013, ApJS, 208, 19
Hirata C. M., Seljak U., 2004, Phys. Rev. D, 70, 063526
Hou J. et al., 2018, MNRAS, 480, 2521
Hou J. et al., 2021, MNRAS, 500, 1201
Ivanov M. M., Simonović M., Zaldarriaga M., 2020, J. Cosmol. Astropart. Phys., 2020, 042
Ivezić Ž. et al., 2019, ApJ, 873, 111
Joudaki S. et al., 2016, MNRAS, 465, 2033
Kaiser N., 1987, MNRAS, 227, 1
Kaiser N., 1992, ApJ, 388, 272
Kaufman G. M., 1967, Center for Operations Research and Econometrics Discussion Paper, 6710, 44
Kazin E. A., Sánchez A. G., Blanton M. R., 2012, MNRAS, 419, 3223
Kilbinger M. et al., 2017, MNRAS, 472, 2126
Kitaura F.-S. et al., 2016, MNRAS, 456, 4156
Kuijken K. et al., 2015, MNRAS, 454, 3500
Laureijs R. et al., 2011, preprint (arXiv:1110.3193)
Lemos P. et al., 2021, MNRAS, 505, 6179
Lewis A., Bridle S., 2002, Phys. Rev. D, 66, 103511
Lewis A., Challinor A., Lasenby A., 2000, ApJ, 538, 473
Lima M., Cunha C. E., Oyaizu H., Frieman J., Lin H., Sheldon E. S., 2008, MNRAS, 390, 118
Limber D. N., 1954, ApJ, 119, 655
Lippich M. et al., 2019, MNRAS, 482, 1786
LoVerde M., Afshordi N., 2008, Phys. Rev. D, 78, 123506
Lyke B. W. et al., 2020, ApJS, 250, 8
Mead A. J., Peacock J. A., Heymans C., Joudaki S., Heavens A. F., 2015, MNRAS, 454, 1958
Miller L. et al., 2013, MNRAS, 429, 2858
Neveux R. et al., 2020, MNRAS, 499, 210
Nishimichi T., Bernardeau F., Taruya A., 2016, Phys. Lett. B, 762, 247
Nishimichi T., Bernardeau F., Taruya A., 2017, Phys. Rev. D, 96, 123515
Percival W. J. et al., 2014, MNRAS, 439, 2531
Perlmutter S. et al., 1999, ApJ, 517, 565
Planck Collaboration XIII, 2016, A&A, 594, A13

Planck Collaboration VI, 2020, A&A, 641, A6
Raveri M., Hu W., 2019, Phys. Rev. D, 99, 043506
Reid B. et al., 2016, MNRAS, 455, 1553
Riess A. G. et al., 1998, AJ, 116, 1009
Riess A. G. et al., 2018, ApJ, 861, 126
Riess A. G., Casertano S., Yuan W., Macri L. M., Scolnic D., 2019, ApJ, 876, 85
Riess A. G. et al., 2021, preprint (arXiv:2112.04510)
Ross A. J. et al., 2020, MNRAS, 498, 2354
Sánchez A. G., 2020, Phys. Rev. D, 102, 123511
Sánchez A. G. et al., 2017, MNRAS, 464, 1640
Sanchez A. G., Ruiz A. N., Gonzalez Jara J., Padilla N. D., 2021, preprint (arXiv:2108.12710)
Scoccimarro R., 2004, Phys. Rev. D, 70, 083007
Sheth R. K., Chan K. C., Scoccimarro R., 2013, Phys. Rev. D, 87, 083002
Smee S. A. et al., 2013, AJ, 146, 32
Smith A. et al., 2020, MNRAS, 499, 269
Tamone A. et al., 2020, MNRAS, 499, 5527
Taruya A., Nishimichi T., Saito S., 2010, Phys. Rev. D, 82, 063522
Taruya A., Bernardeau F., Nishimichi T., Codis S., 2012, Phys. Rev. D, 86, 103528
Tröster T. et al., 2020, A&A, 633, L10
Tröster T. et al., 2021, A&A, 649, A88
York D. G. et al., 2000, AJ, 120, 1579
Zarrouk P. et al., 2018, MNRAS, 477, 1639
Zhao C. et al., 2021, MNRAS, 503, 1149
Zheng Z., Coil A. L., Zehavi I., 2007, ApJ, 667, 760

APPENDIX A: JOINT ANALYSIS WITH KIDS-450 DATA

In this section, we present the joint analysis of the anisotropic clustering measurements from BOSS and eBOSS together with cosmic shear measurements from KiDS-450 (Hildebrandt et al. 2016).

We use cosmic shear measurements from the Kilo-Degree Survey, (Kuijken et al. 2015; Hildebrandt et al. 2016; Fenech Conti et al. 2017), hereafter referred to as KiDS. The KiDS data are processed by THELI (Erben et al. 2013) and Astro-WISE (Begeman et al. 2012; de Jong et al. 2017). Shears are measured using lensfit (Miller et al. 2013), and photometric redshifts are obtained from PSF-matched
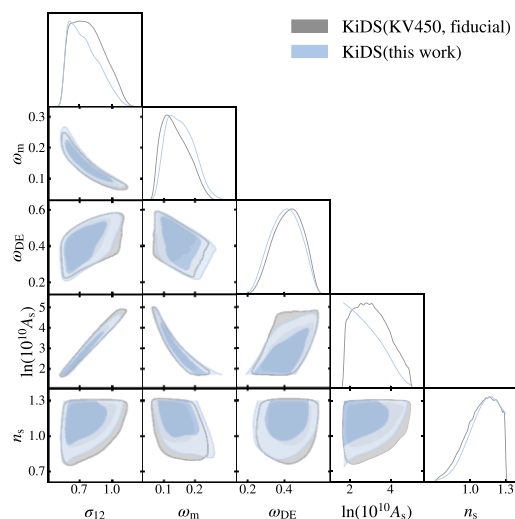

Figure A1. Comparison of the marginalized posterior distributions between the fiducial KV450 analysis and this work. For this comparison, we adapted the cosmological parameter priors to match those of the fiducial analysis.

photometry and calibrated using external overlapping spectroscopic surveys (see Hildebrandt et al. 2016).

The KiDS-450 weak lensing data set consists of tomographic shear measurements from four redshift bins spanning the total range of $0.1 < z \leq 0.9$ and the corresponding source redshift distributions estimated from the weighted direct calibration ('DIR') for each bin (Lima et al. 2008). We use the recommended scale cuts and use the angular bins with $\theta < 72\,\mathrm{arcmin}$ for $\xi_+(\theta)$ and $\theta > 6\,\mathrm{arcmin}$ for $\xi_-(\theta)$.

It is important to note that here we are using the same DES shear model as in the main analysis. This means that the treatment of the nuisance parameters (namely, the baryonic effects, the photometric redshift uncertainty, and the additive and multiplicative bias parameters) differs from the original analysis of KiDS-450. We do not include baryonic effects and our priors for photometric redshift uncertainty match those of Hildebrandt, H. et al. (2020). We impose flat priors for multiplicative bias $U(-0.1, 0.1)$ with the additive bias parameter taken to be zero, mimicking the DES set up. Finally, we also follow the DES intrinsic alignment model, imposing a flat prior on redshift evolution of intrinsic alignment parameter. We compare our final posteriors with the ones obtained from the publicly available KV450 chains (Hildebrandt et al. 2020) and find a good agreement between the two, as shown in Fig. A1. Moreover, there is a weak tendency is for our analysis to prefer lower RMS variance values, which leads to a more conservative assessment of any potential tensions with *Planck*.

Fig. A2 shows the combined constraints from the combination of KiDS-450 + BOSS +eBOSS (orange contours), which are in near-perfect agreement with the equivalent combination using
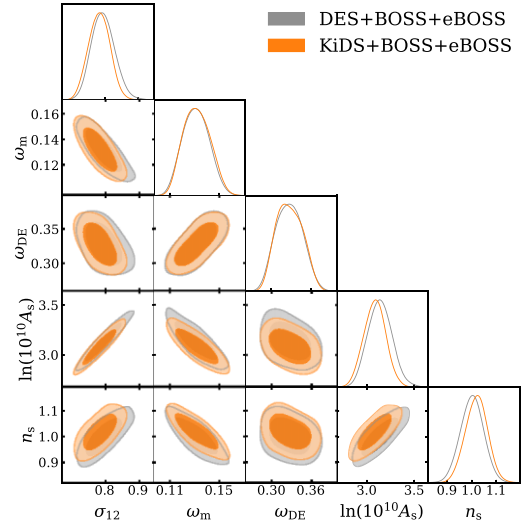
Figure A2. Comparison of low-redshift constraints obtained by combining BOSS + eBOSS with either DES Y1 3 × 2pt data (grey contours) or the KiDS-450 shear measurements (orange contours).

DES (grey contours). The suspiciousness statistic shows an agreement between *Planck* and this set of low-redshift measurements of $1.5 \pm 0.5\sigma$, which is also consistent with our results from BOSS + eBOSS + DES.

This paper has been typeset from a T$_{\mathrm{E}}$X/L^{A}T$_{\mathrm{E}}$X file prepared by the author.